

**NASA
Technical
Paper
2705**

**AVSCOM
Technical
Report
86-C-42**

April 1987

**Vibration Characteristics
of OH-58A Helicopter
Main Rotor Transmission**

David G. Lewicki
and John J. Coy

AVSCOM REPORT 86-C-42
NASA TECHNICAL PAPER 2705
APRIL 1987
VIBRATION CHARACTERISTICS
OF OH-58A HELICOPTER
MAIN ROTOR TRANSMISSION
DAVID G. LEWICKI
AND JOHN J. COY



**NASA
Technical
Paper
2705**

**AVSCOM
Technical
Report
86-C-42**

1987

**Vibration Characteristics
of OH-58A Helicopter
Main Rotor Transmission**

David G. Lewicki
and John J. Coy

*Propulsion Directorate
USAARTA-AVSCOM
Lewis Research Center
Cleveland, Ohio*

NASA

National Aeronautics
and Space Administration

Scientific and Technical
Information Branch

Summary

Experimental vibration tests were performed on the OH-58A helicopter main rotor transmission. The tests were conducted in the 500-hp helicopter transmission test stand at NASA Lewis. Seven accelerometers were mounted at various locations on the transmission housing. The testing consisted of a matrix of torque and speed conditions covering transmission input torques of 176 to 352 N-m (1559 to 3119 lb-in.) and transmission input speeds of 3000 to 6000 rpm. Accelerometer signals were analyzed by using Fourier spectra, power spectral density functions, and averaging techniques.

The Fourier spectra analysis showed vibration amplitude peaks occurring at the spiral bevel and planetary gear mesh harmonics. The highest magnitude of vibration was at the spiral bevel gear meshing frequency. Harmonic sideband frequencies for both the spiral bevel mesh and the planetary mesh occurred at multiples of the planet passing frequency. Accelerometer root-mean-square (rms) average vibration levels were also determined. Transmission speed had a significant effect on rms vibration levels, but transmission torque had a small effect. At the same speed and torque conditions, measured vibration levels were different at different locations but the same for different measurement directions at the same location. Spiral bevel mesh and planetary mesh vibration contributions were determined by using power spectral density functions. There was, however, no trend as to the effect of torque or speed on spiral bevel mesh or planetary mesh vibration contributions as a percentage of total vibration.

Introduction

Helicopter noise and vibration are important topics because of health and environment concerns, passenger comfort, and pilot efficiency. Both external and internal noise create concern. External noise is due to the rotor blades and the engine inlet and exhaust; internal noise is attributed to transmission vibration, and in particular, to the gears. The standard approach to quieting the helicopter interior is to add cabin acoustic material. The corresponding weight penalty opposes the goal of ever-increasing power-to-weight ratios for helicopter drive systems.

As power increases so does the weight penalty associated with cabin soundproofing materials (ref. 1). This has led to an effort to reduce noise and vibration at their origin.

Transmissions are the main source of noise in today's helicopter interiors, with the noise originating from the gear mesh (ref. 2). Gear tooth or shaft deflections, gear tooth profile errors, or gear or bearing misalignments can lead to dynamic loads, vibration, and noise (refs. 3 and 4). In addition to the annoyance of transmission noise, lack of vibration control near resonant frequencies can lead to damaging transmission failures (refs. 5 and 6).

Vibration and temperature tests were performed on the main rotor transmission for the OH-58A U.S. Army light observation helicopter (ref. 7). Spectrum analyses showed the dominant sources of vibration to be the spiral bevel gear mesh and the planetary gear mesh. For normal operating conditions the highest vibration amplitude occurred at the spiral bevel meshing frequency. Transmission vibration tests were also performed on larger helicopters (refs. 8 and 9). Quite high vibration levels are associated with these transmissions, and methods to reduce noise and vibration are being developed (refs. 1, 10, and 11).

The objective of the present study was to measure vibration data for the OH-58A main rotor helicopter transmission. The results can serve as baseline data for comparison with measured results from future technological improvements in component and total system design, manufacturing techniques, or materials. Experimental vibration tests were performed on the OH-58A transmission over a range of torque and speed conditions at NASA Lewis. Vibration results are presented as Fourier spectra and average accelerations.

Apparatus

OH-58A Main Rotor Transmission

The OH-58A is a single-engine, land-based light observation helicopter. The helicopter serves both military (OH-58A Kiowa) and commercial (Bell Model 206 Jet Ranger) needs. The OH-58A main rotor transmission (fig. 1) is rated for use at an engine output of 210-kW (270-hp) continuous power at 6180 rpm and 236 kW (317 hp) for 5 min at takeoff (ref. 7). The transmission is a two-stage reduction gearbox. For the first stage the input shaft drives a 19-tooth spiral bevel pinion gear, which meshes with a 71-tooth gear. The bevel pinion shaft is mounted on triplex ball bearings and one roller bearing. The bevel gear shaft is mounted on duplex ball bearings and one roller bearing.

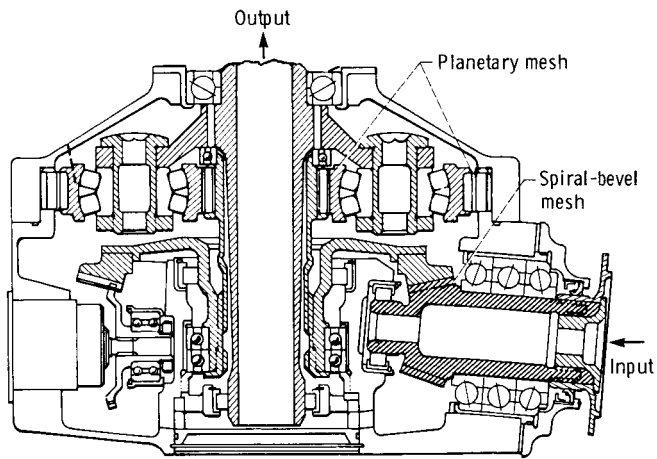


Figure 1.—OH-58A helicopter main rotor transmission.

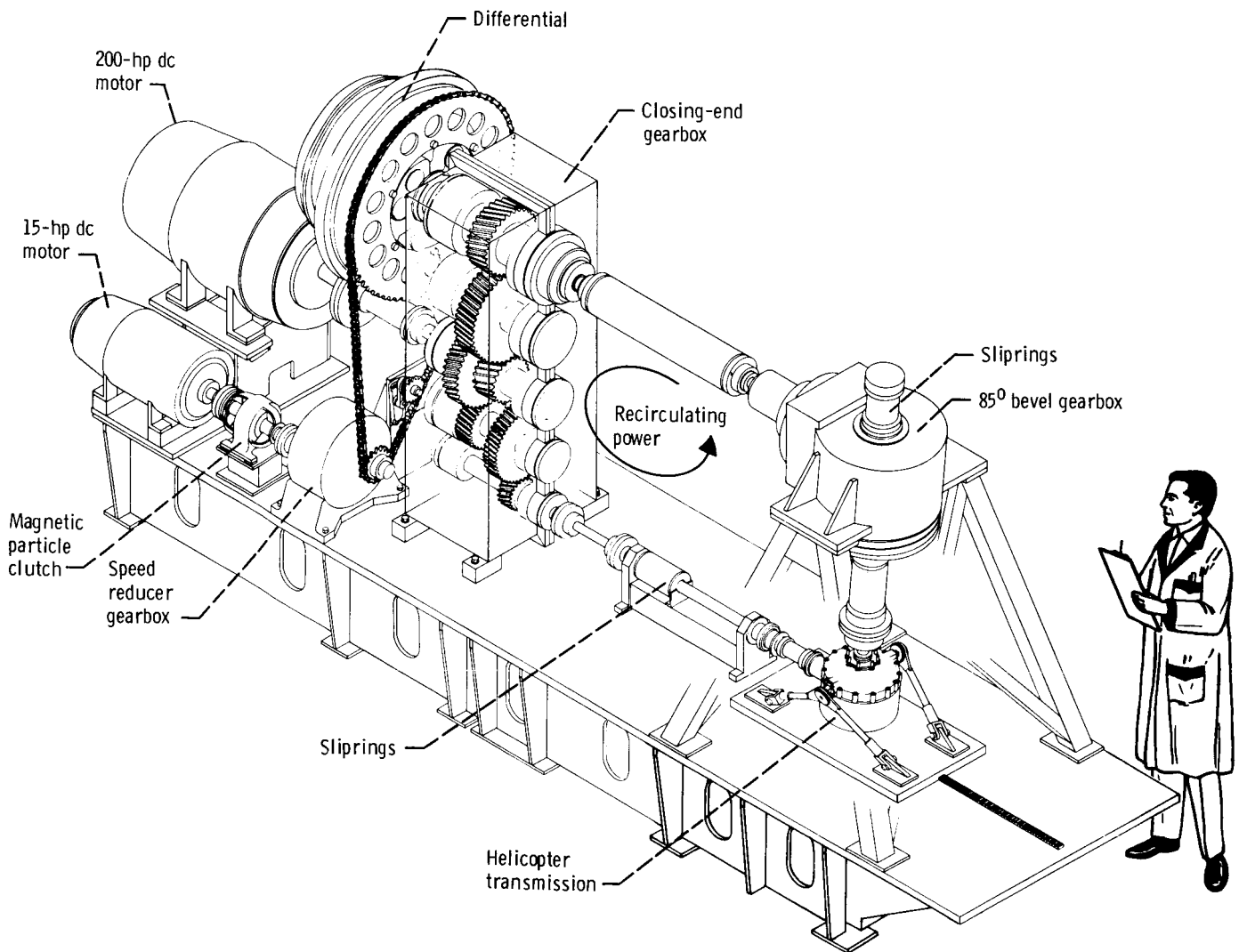


Figure 2.—NASA Lewis 500-hp helicopter transmission test stand.

A planetary mesh provides the second reduction stage. The bevel gear shaft is splined to a sun gear shaft. The 27-tooth sun gear drives three 35-tooth planet gears. The planet gears mesh with a 99-tooth fixed ring gear, which is splined to the top case. The planet gears are mounted on double-row spherical roller bearings; the bearings are attached to the planet carrier. Power is taken out through the planet carrier, which is splined to the mast output shaft. The output shaft is supported by a ball bearing and a roller bearing. The overall reduction ratio of the main power train is 17.44:1.

The 71-tooth bevel gear also drives a 27-tooth accessory gear. The accessory gear runs an oil pump, and lubrication is supplied through jets located in the top case.

NASA Lewis Test Stand

Vibration tests were performed in the NASA Lewis 500-hp helicopter transmission test stand (fig. 2). The test stand operates on the "four square" or torque-regenerative principle. Mechanical power is recirculated through a closed loop of gears and shafting, one of which is the test transmission. In the test stand the output of the test transmission is attached to the bevel gearbox. The output shaft of the bevel gearbox passes through a hollow shaft in the closing-end gearbox and is connected to the differential gearbox. The output of the differential is attached to the hollow shaft in the closing-end gearbox. The output of the closing-end gearbox is connected to the input of the test transmission, thereby closing the loop.

A 149-kW (200-hp) direct-current (dc) motor powers the test stand and controls the speed. The motor output is attached to the closing-end gearbox. Only losses due to friction are replenished by the motor since power is recirculated around the loop.

An 11-kW (15-hp) dc motor provides the torque in the closed loop. The motor drives a magnetic particle clutch. The clutch output does not turn but exerts a torque through a speed reducer gearbox and a chain drive to a large sprocket on the differential gearbox. The torque on the sprocket puts a torque in the differential gearbox, which in turn, provides the torque in the closed loop. The magnitude of torque in the loop is adjusted by changing the electric field strength of the magnetic particle clutch.

The test transmission input and output shafts are equipped with speed sensors, torquemeters, and sliprings. Test transmission lubrication is supplied by an internal oil pump. The transmission oil can be cooled by a flight hardware air/oil cooler mounted on the transmission (with forced air provided to the cooler) or by an external oil/water heat exchanger. An external oil-pumping system located in the basement below the test stand room is also available for the test transmission.

The 149-kW (200-hp) motor is equipped with a speed sensor and a torquemeter. The magnetic particle clutch is equipped with speed sensors on the input and output shafts and with thermocouples. A facility oil-pumping and cooling system

lubricates the differential gearbox, the closing-end gearbox, and the bevel gearbox. The facility gearboxes are also equipped with accelerometers and thermocouples for health monitoring.

Instrumentation and Testing Procedure

Seven piezoelectric accelerometers were mounted on the OH-58A transmission housing (table I, fig. 3). The accelerometers were located on the right and left trunnion mounts, the input bevel pinion gear housing, and the ring gear

TABLE I.—OH-58A TRANSMISSION ACCELEROMETER LOCATIONS

[See also fig. 3.]

Accelerometer	Location	Direction
1	Ring gear housing	45° Transverse-longitudinal
2	Right trunnion mount	Transverse
3	Right trunnion mount	Longitudinal
4	Right trunnion mount	Vertical
5	Input bevel gear housing	Transverse
6	Input bevel gear housing	Vertical
7	Left trunnion mount	Vertical

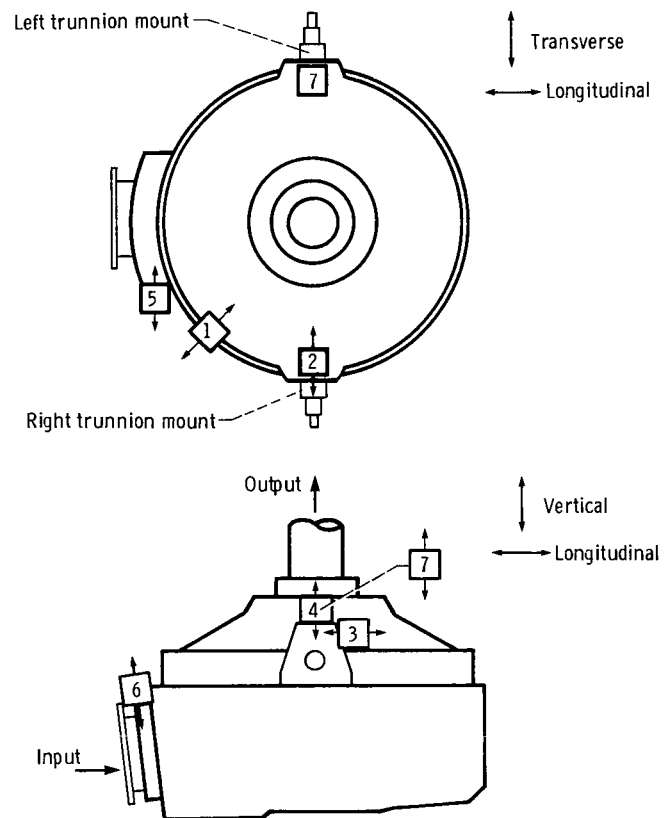


Figure 3.—Accelerometer locations on OH-58A transmission.

housing. Each accelerometer measured vibration in only one direction. The various accelerometers were located, however, to cover all three directions: vertical, longitudinal, and transverse. The frequency response of the accelerometers was ± 5 percent charge from 2 to 5500 Hz and +20 percent charge at 10 kHz. The accelerometer resonant frequency was 27 kHz.

The vibration measurement system was the same for all accelerometers (fig. 4). The accelerometer produced a charge output proportional to acceleration. The output was fed to a charge amplifier that produced both alternating current (ac) voltage and dc voltage. The ac signal, which represented the actual acceleration as a function of time, was stored on tape and later retrieved for processing with a Fourier analyzer. The dc signal, which represented an average acceleration, was converted to digital format by the data reduction system for computer processing. The dc signal also served as a health-monitoring channel to check for possible high vibration levels.

The test procedure was as follows: First, all instrumentation checks on operation, calibration, and settings were made. Next, calibration signals were placed on the recording tape. All safety interlocks and automatic shutdown devices were tested. The fan blower for the transmission oil cooler and then the main drive motor were turned on. The transmission input speed was increased to approximately 2000 rpm in order to circulate oil throughout the transmission. A nominal amount of torque load was applied, and then speed and torque were adjusted to arrive at the desired condition for testing. The

TABLE II.—VIBRATION TEST OPERATION CONDITIONS

Test	Input torque			Input speed		Power,	
	N-m	lb-in.	Percent of full rated	rpm	Percent of full rated	kW	hp
1	352	3119	96.5	6060	98.1	224	300
2	323	2859	88.4	↓	↓	205	275
3	294	2599	80.4			186	250
4	264	2339	72.3			168	225
5	235	2079	64.3			149	200
6	206	1819	56.3			130	175
7	176	1559	48.2	↓	↓	112	150
8	352	3119	96.5	6000	97.1	221	297
9	↓	↓	↓	5500	89.0	203	272
10				5000	80.9	184	247
11				4500	72.8	166	223
12				4000	64.7	148	198
13				3500	56.6	129	173
14				3000	48.5	110	148

transmission was run until the oil outlet temperature was stabilized (66 to 82 °C; 150 to 180 °F). This usually required 15 to 20 min. When equilibrium conditions for speed, load, and temperature were achieved, the vibration data were collected.

Tests were performed over a range of torques and speeds (table II). The transmission input torque was varied from 48 to 97 percent of the engine full-rated value (365 N-m; 3233 lb-in.). The transmission input speed was varied from 49 to 97 percent of the full-rated value (6180 rpm).

Results and Discussion

Gear Mesh Harmonic Frequencies

The fundamental meshing frequency for a spiral bevel gear pair is

$$f_b = \frac{\omega N}{60} \quad (1)$$

where N is the number of gear teeth (driver or driven) and ω is the gear speed in revolutions per minute. (Symbols are defined in the appendix.) A similar relationship holds true for a planetary mesh with the sun gear as input, the ring gear fixed, and the planet carrier as output. The fundamental planetary meshing frequency is

$$f_p = \frac{\omega_s N_s}{60} \left(\frac{N_r}{N_s + N_r} \right) \quad (2)$$

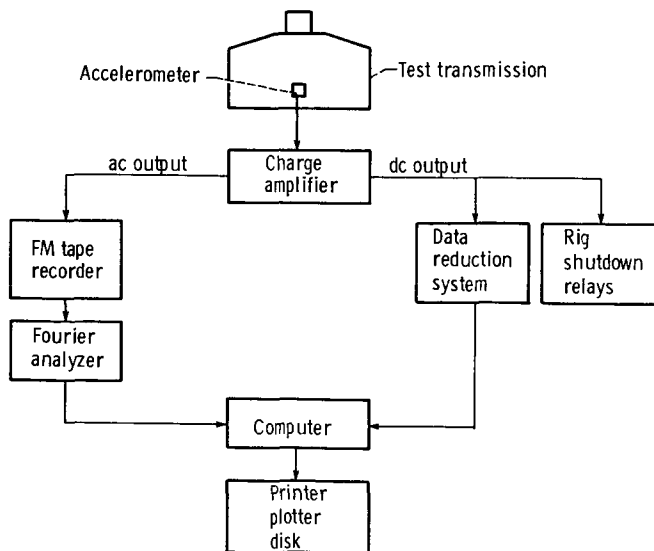


Figure 4.—Vibration measurement system.

TABLE III.—OH-58A TRANSMISSION
SPIRAL BEVEL MESH AND
PLANETARY MESH HARMONIC
FREQUENCIES

[Input speed, 6060 rpm.]

Harmonic	Spiral bevel mesh	Planetary mesh
	Harmonic frequency, Hz	
Fundamental	1919	573
2nd	3838	1147
3rd	5757	1720
4th	7676	2294
5th	9595	2867
6th		3440
7th		4014
8th		4587
9th		5160
10th		5734
11th		6307
12th		6881
13th		7454
14th		8027
15th		8601
16th		9174
17th		9748

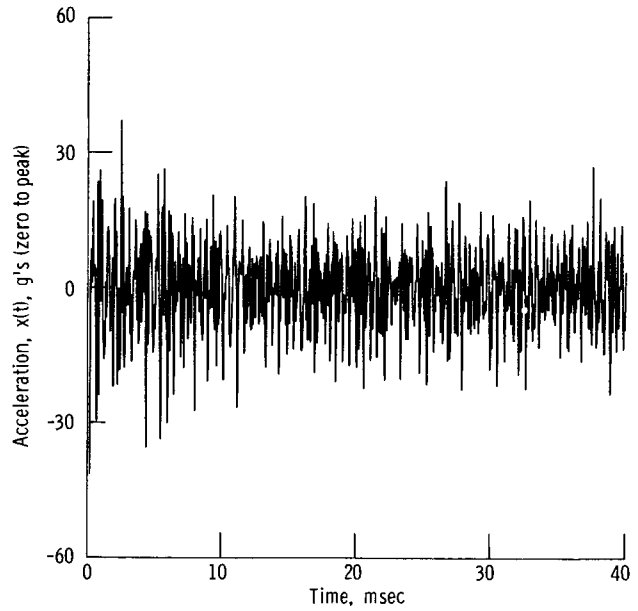


Figure 5.—Time trace of accelerometer 1 (ring gear housing).

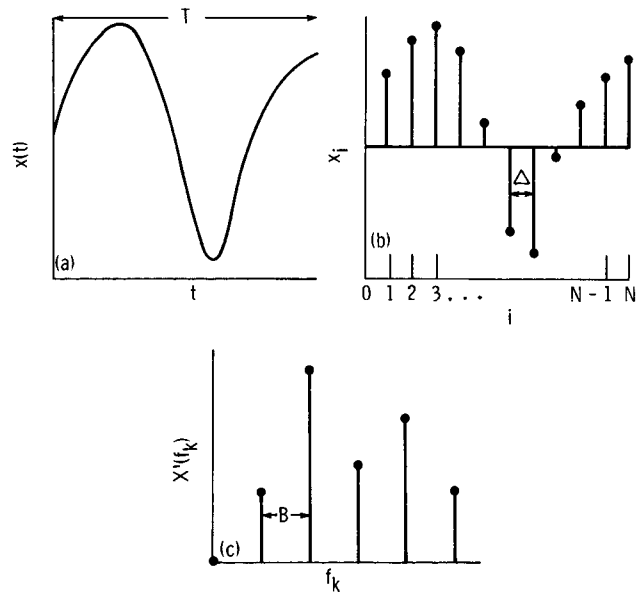
where N_s is the number of sun gear teeth, N_r is the number of ring gear teeth, and ω_s is the sun gear speed in revolutions per minute. The term in parentheses relates the sun gear rotation to a fixed planet carrier system. This is needed to account for planet gear relative rotation. Note that the meshing frequency of equation (2) applies for a sun gear meshing with a planet gear as well as for a planet gear meshing with a ring gear.

Harmonic frequencies are defined as integer multiples of the fundamental frequency. The second harmonic is two times the fundamental frequency, the third harmonic is three times the fundamental frequency, and so on. For the OH-58A transmission the spiral bevel mesh has 5 harmonics and the planetary mesh has 17 harmonics in the 0- to 10-kHz range at an input speed of 6060 rpm (table III).

Fourier Spectra

The typical accelerometer response as a function of time was quite irregular (fig. 5). The response was converted from the time domain to the frequency domain by using a Fourier transformation. Thus the erratic vibration was broken down into its harmonic components.

Accelerometer acceleration $x(t)$, a continuous function of time t (fig. 6(a)), can be approximated by x_i through use of a discrete number of points (fig. 6(b)), where



(a) Continuous function—time domain.
(b) Discrete function—time domain.
(c) Discrete Fourier transform—frequency domain.

Figure 6.—Discrete Fourier transform.

$$i = \frac{t}{N} \quad (3)$$

$$\Delta = \frac{T}{N} \quad (4)$$

T is the time period, and N is the number of intervals. The bandwidth B is defined as

$$B = \frac{1}{T} \quad (5)$$

Assuming x_i is periodic with T , the real portion of the discrete Fourier transform (DFT) from reference 12 is

$$a_k = \frac{1}{N} \sum_{i=0}^{N-1} x_i \cos\left(\frac{2\pi ki}{N}\right) \quad (6)$$

and the imaginary portion of the DFT is

$$b_k = \frac{1}{N} \sum_{i=0}^{N-1} x_i \sin\left(\frac{2\pi ki}{N}\right) \quad (7)$$

where k is an integer from 0 to $N - 1$. The magnitude factor $X'(f_k)$ is defined as

$$X'(f_k) = (a_k^2 + b_k^2)^{1/2} \quad (8)$$

and is a function of frequency f_k , where

$$f_k = \frac{k}{T} \quad (9)$$

as shown in figure 6(c).

The data signals were conditioned to avoid aliasing such that

$$f_k < \frac{1}{2\Delta} \quad (10)$$

where f_K was the maximum frequency component in $x(t)$ (aliasing is the production of nonexistent frequency components in the DFT). Also, k ranged from 0 to K , where

$$K = Tf_K \quad (11)$$

The OH-58A accelerometer ac outputs were retrieved from tape and fed to a spectrum analyzer. The spectrum analyzer performed a fast Fourier transform (FFT). The FFT is an efficient computer algorithm for calculating discrete Fourier transforms (ref. 12). The analyzer output was a magnitude factor $X(f_k)$, where

$$X(f_k) = \sqrt{2}X'(f_k) \quad (12)$$

The analyzer was set for $f_K = 10$ kHz. Internally the analyzer used $N = 1024$ intervals, and for $f_K = 10$ kHz the analyzer had a time period of $T = 0.04$ sec. This produced a bandwidth B of 25 Hz, a time interval between samples Δ of 3.91×10^{-5} sec, and $K = 400$ intervals for the frequency domain. The analyzer was also set for Hanning windowing. The windowing function modified the acceleration time waveform x_i by weighting the waveform so that the beginning and ending points reduced to zero. The weighting reduced the distortion caused by finite record samples of the FFT process and nonperiodic acceleration waveforms.

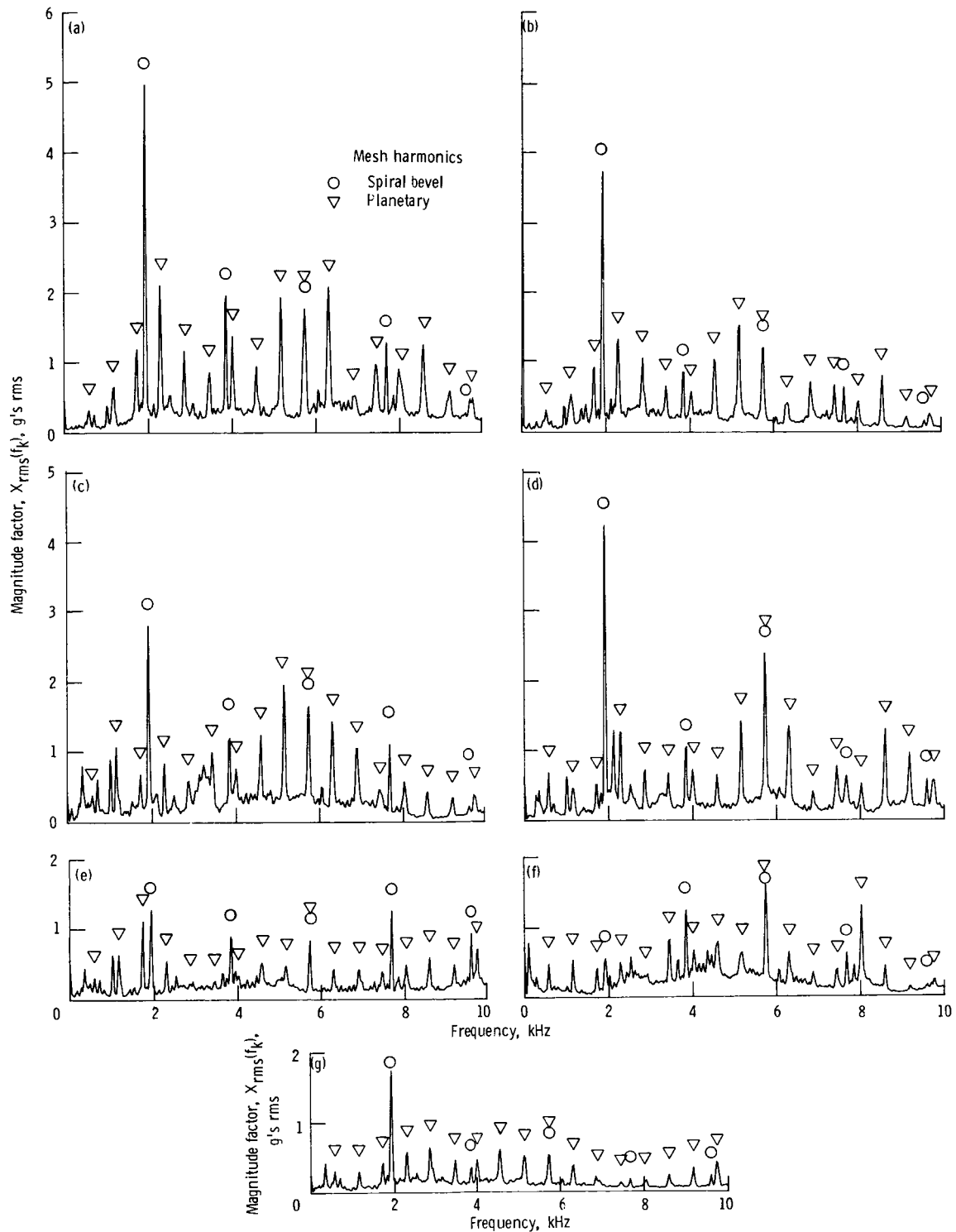
The analyzer also performed an rms averaging technique on the magnitude factor to smooth the signal variations with time. At each frequency the average magnitude factor was composed of 50 readings, where

$$X_{\text{rms}}(f_k) = \left[\frac{1}{50} \sum_{j=1}^{50} X_j^2(f_k) \right]^{1/2} \quad (13)$$

Accelerometer 1 (on the ring gear housing) produced the highest levels of vibration. From the Fourier transformation the dominant vibration sources were the spiral bevel mesh and the planetary mesh (fig. 7(a)). Vibration amplitude spikes occurred at the spiral bevel mesh and planetary mesh harmonic frequencies. The highest vibration amplitude was at the spiral bevel fundamental meshing frequency.

The vibration spectra of accelerometers 2 to 4 (on the right trunnion mount, figs. 7(b) to (d)) were similar in trend to that of accelerometer 1. Spikes occurred at the spiral bevel mesh and planetary mesh harmonics, and the highest amplitude was at the spiral bevel fundamental frequency. Note that figures 7(b) to (d) are rather similar, implying that the measured vibration was not significantly affected by the measurement direction.

The vibration spectra of accelerometers 5 and 6 (on the input bevel gear housing, figs. 7(e) and (f)) had lower vibration levels than the other spectra. The spiral bevel harmonics were the dominant vibration sources, but the large amplitude at the spiral bevel fundamental frequency did not occur. Accelerometer 7 (on the left trunnion mount, fig. 7(g)) had trends



(a) Accelerometer 1 (ring gear housing). (b) Accelerometer 2 (right trunnion mount, transverse).
 (c) Accelerometer 3 (right trunnion mount, longitudinal). (d) Accelerometer 4 (right trunnion mount, vertical).
 (e) Accelerometer 5 (input bevel gear housing, transverse). (f) Accelerometer 6 (input bevel gear housing, vertical).
 (g) Accelerometer 7 (left trunnion mount, vertical).

Figure 7.—Vibration spectra. Input speed, 6060 rpm; input torque, 352 N-m (3119 lb-in.).

similar to that of the right trunnion mount. The vibration levels, however, were only about half those of the right trunnion mount.

Gear vibration spectra may possess sidebands about the fundamental and harmonic frequencies (ref. 13). Sidebands result from amplitude modulation and frequency modulation. Amplitude modulation occurs when excitation force amplitudes vary with time, such as for eccentric gears. Frequency modulation results when mesh frequencies change with time, such as for gears with tooth spacing errors or torsional vibration. Sidebands usually occur at frequencies of

$$f_{\text{side}} = f_m \pm n f_s \quad (14)$$

where f_m is a fundamental or harmonic meshing frequency, f_s is the gear shaft frequency (driver or driven), and n is an integer (1,2,3,...).

For planetary meshes sidebands may also occur at multiples of the planet passing frequency, where

$$f_{\text{side}} = f_m \pm n f_{pp} \quad (15)$$

$$f_{pp} = \frac{\omega_s}{60} \left(\frac{N_s}{N_s + N_r} \right) P \quad (16)$$

and P is the number of planet gears. Equation (16) is valid for a fixed-ring planetary with the sun gear as input and the planet carrier as output.

The OH-58A planet passing frequency at 6060-rpm input speed is 17 Hz. The sidebands for the spiral bevel mesh and the planetary mesh occurred at multiples of the planet passing frequency (fig. 8). Very few sidebands correlating to amplitude or frequency modulation were found (using a linear scale on the Fourier transformation). This implies high-quality gears and high-accuracy installation. Note that the sideband frequencies were determined by using a zoom feature of the spectrum analyzer. The zoom feature basically increases the time period of the time domain signal (by sampling more points), and this, in turn decreases the bandwidth. In determining the sideband frequencies of figure 8, $B = 0.625$ Hz was used. Also note that rms averaging was not used.

Average Vibration

The rms average acceleration on the time trace is defined as

$$x_{\text{rms}} = \left(\lim_{T \rightarrow \infty} \frac{1}{T} \int_0^T x^2(t) dt \right)^{1/2} \quad (17)$$

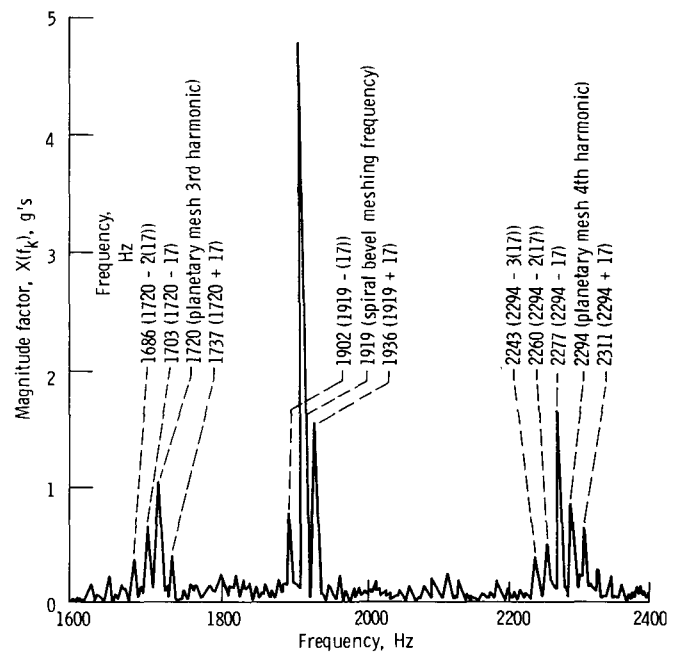


Figure 8.—Zoom vibration spectrum of accelerometer 1 (ring gear housing, fig. 6(a)). Input speed, 6060 rpm; input torque, 352 N-m (3119 lb-in.); planet passing frequency, 17 Hz.

For a time trace of length T the rms acceleration can be approximated by considering discrete points where

$$x_{\text{rms}} \approx \left(\frac{1}{I} \sum_{i=1}^I x_i^2 \right)^{1/2} \quad (18)$$

and I is the total number of points.

The OH-58A acceleration time traces (fig. 5 as an example) were retrieved from tape, fed to the spectrum analyzer, and routed to a computer for rms average calculations. The time interval between samples Δ and the total number of points I were varied in hopes of optimizing the data collection. The analyzer had a finite number of time intervals available ($\Delta = 3.906, 7.813, 15.625, 19.531 \mu\text{sec}$, etc.). A time interval of $15.625 \mu\text{sec}$ was chosen. For $\Delta > 15.625 \mu\text{sec}$ the digital approximations failed to encompass all the time trace peaks. This led to a lower-than-actual rms calculation, regardless of the total number of points taken. For $\Delta < 15.625 \mu\text{sec}$ the rms calculations required more data points for convergence than calculations with $\Delta = 15.625 \mu\text{sec}$.

Data were collected in sets of 31 744 points (the maximum allowed for the analyzer-computer software). The rms average based on the cumulation of five sets compared with the rms average based on the cumulation of four sets usually produced

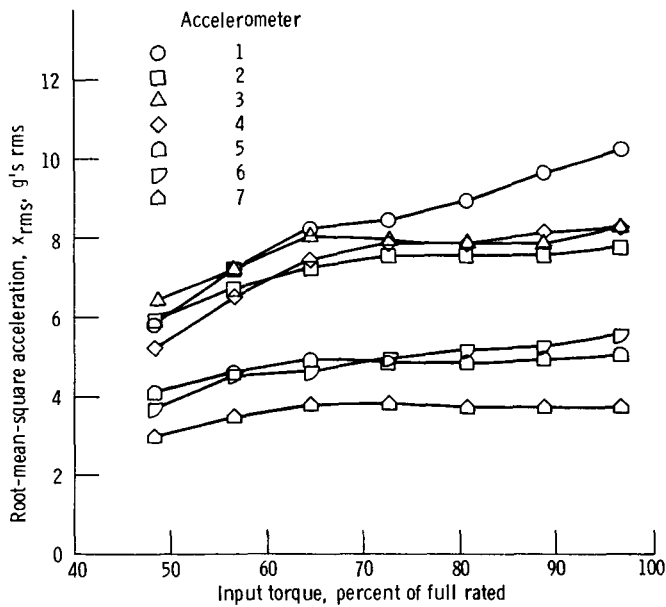
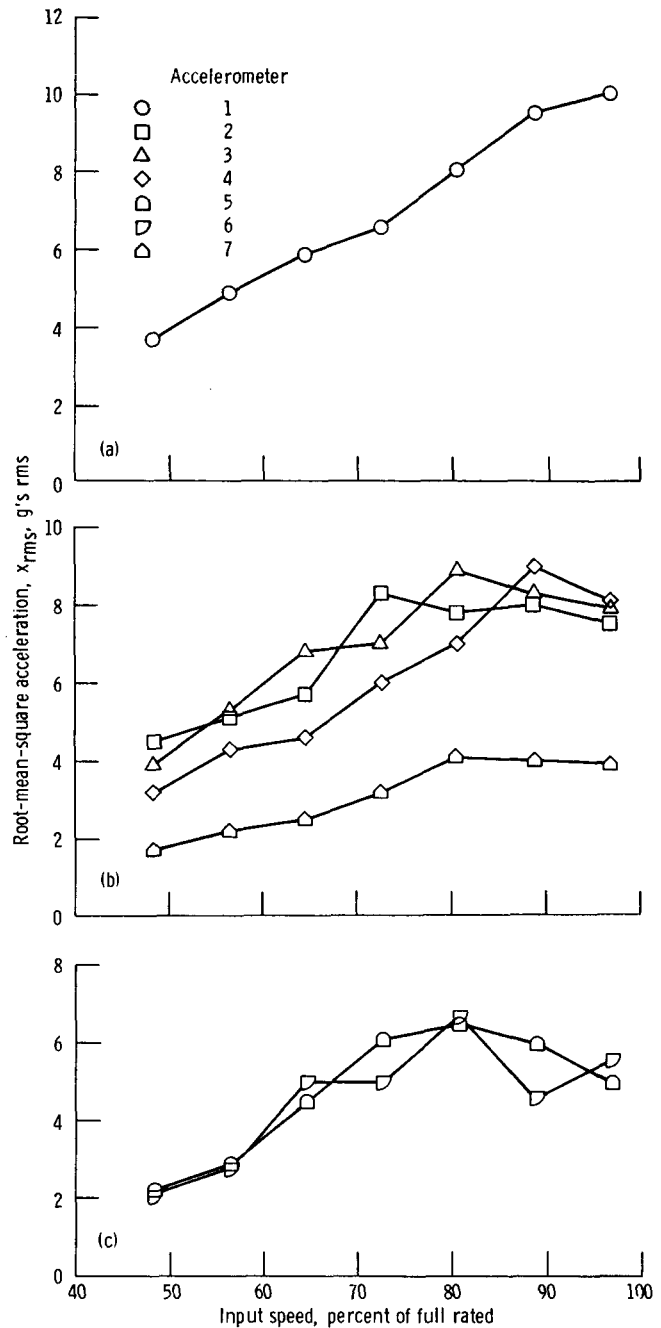


Figure 9.—Effect of torque on vibration.

an error of less than 1 percent. Thus for each test condition of table II five sets for each accelerometer were accumulated. Five sets of 31 744 points each and $\Delta = 15.625 \mu\text{sec}$ gave total points I of 158 720 and a total time period T of 2.48 sec.

Torque had a small effect on vibration (fig. 9). For all accelerometers the vibration increased with torque for torques from 50 to 65 percent of full rated. Above 65 percent the vibration was fairly constant. Accelerometer 1 (on the ring gear housing) was the only exception. For this accelerometer vibration increased with torque for the full range of torques tested. Note that accelerometers located in the same locations but measuring in different directions (2 to 4 on the right trunnion mount; 5 and 6 on the input bevel gear housing) had similar results. This implies that measurement direction had a small effect on measured vibration. Also, the measured vibration levels were different depending on measurement location as some locations (such as the right trunnion mount, accelerometers 2 to 4) had higher vibration levels than others (such as the left trunnion mount, accelerometer 7). Note that the vibration levels of accelerometers 4 and 7 are different even though the mounting geometry is symmetric. One explanation is the nonsymmetric loading that the transmission sees.

Speed significantly affected vibration (fig. 10). Vibration continued to increase with speed for accelerometer 1 (the ring gear housing, fig. 10(a)). For all other accelerometers vibration increased with speed until a resonant point was reached (figs.



(a) Accelerometer 1.

(b) Accelerometers 2, 3, 4, and 7.

(c) Accelerometers 5 and 6.

Figure 10.—Effect of speed on vibration.

10(b) and (c)). Then it usually decreased slightly as speed increased above the resonance. In addition, the measured resonant speed differed with measurement location and direction.

TABLE IV.—LINEAR CURVE FITS OF
rms AVERAGE ACCELERATION
CALCULATIONS

Accelerometer	Tests 1 to 7 ^a		Tests 8 to 14 ^b	
	m_1	b_1	m_2	b_2
1	0.083	2.32	0.140	-2.91
2	.032	4.78	.075	1.27
3	.028	5.56	.089	.42
4	.056	3.24	.120	-2.49
5	.014	3.70	.073	-.59
6	.032	2.44	.070	-.53
7	.011	2.83	.052	-.71

$$x_{rms}^a = m_1 (\text{percent torque}) + b_1$$

$$x_{rms}^b = m_2 (\text{percent speed}) + b_2$$

A curve-fitting analysis was performed on the rms average results. For each accelerometer the rms acceleration as a function of torque was approximated linearly by using a least-squares fit. For most accelerometers the linear fit was a reasonable approximation. There was, however, no consistency between accelerometers as the curve-fit results of the various accelerometers had different slopes and intercepts (table IV).

Power Spectral Density

The one-sided power spectral density function from reference 14 is

$$G(f_k) = 2TX'(f_k)^2 \quad (19)$$

From equations (5) and (12)

$$G(f_k) = \frac{X(f_k)^2}{B} \quad (20)$$

The power spectral density, a function of the frequency domain, is related to the time domain by

$$x_{rms}^2 = B \sum_{k=0}^{K-1} G(f_k) \quad (21)$$

The right side of equation (21) is the area under the power spectral density curve. Thus from equations (20) and (21) the area under the analyzer frequency-magnitude factor curve is related to the mean-square acceleration. By using this concept the vibration contributions of the spiral bevel mesh and the planetary mesh were determined.

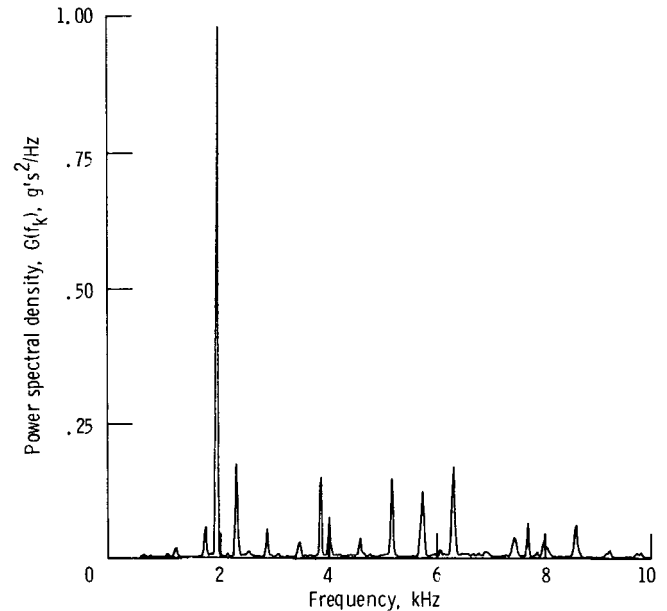


Figure 11.—Power spectral density function—accelerometer 1 (ring gear housing, fig. 6(a)). Input speed, 6060 rpm; input torque, 352 N-m (3119 lb-in.).

The power spectral density function (eq. (20)) was determined for each accelerometer at each test condition of table II (fig. 11 as an example). The areas under the curve for the individual harmonics were calculated by using a trapezoidal approximation. Each trapezoid was one bandwidth wide (for the analyzer $B = 25$ Hz for a 0- to 10-kHz frequency range). The area for a harmonic consisted of three to four trapezoids (75 to 100 Hz) to account for sideband contributions. For each accelerometer and test condition the values of the areas under the power spectral density function for the spiral bevel harmonics were added together and divided by the total area under the power spectral density function. This produced the spiral bevel mesh vibration contribution in terms of percent of mean-square acceleration. The same was done for the planetary mesh harmonics.

There was no apparent trend as to the effect of torque and speed on spiral bevel mesh and planetary mesh vibration contributions as a percentage of total vibration for the various accelerometers (figs. 12 and 13). The torque-vibration curves (fig. 12) in general were smooth, but the speed-vibration curves (fig. 13) were jagged. In many cases the spiral bevel mesh and planetary mesh vibration contributions were fairly constant with respect to torque for torques from 55 to 90

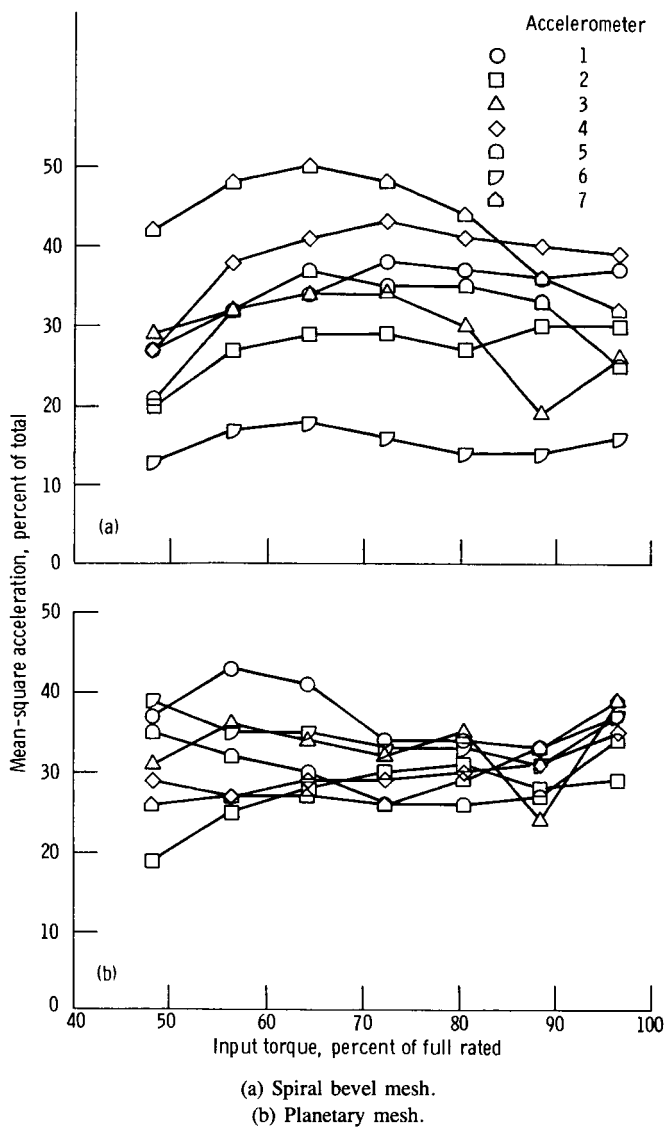


Figure 12.—Effect of torque on vibration contribution.

percent of full rated (fig. 12(a), accelerometers 1, 2, 4, and 6; fig. 12(b), accelerometers 1, 2, 4, 5, and 7). The spiral bevel mesh and planetary mesh vibration contributions increased and decreased randomly with respect to speed.

There was also no apparent trend as to whether the spiral

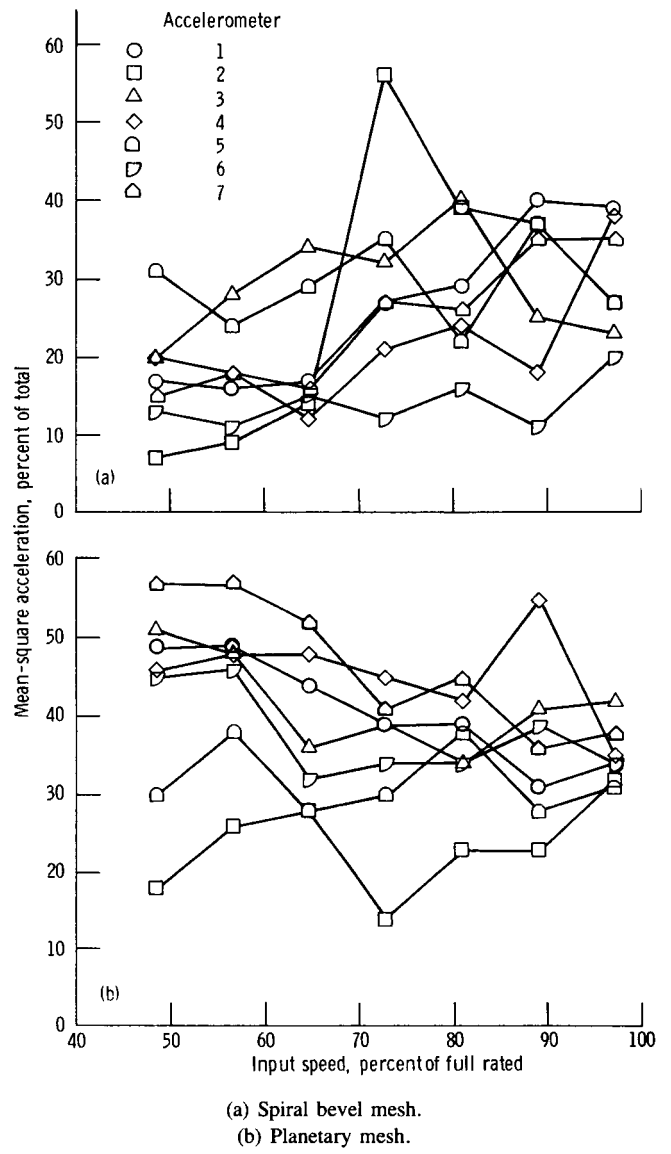
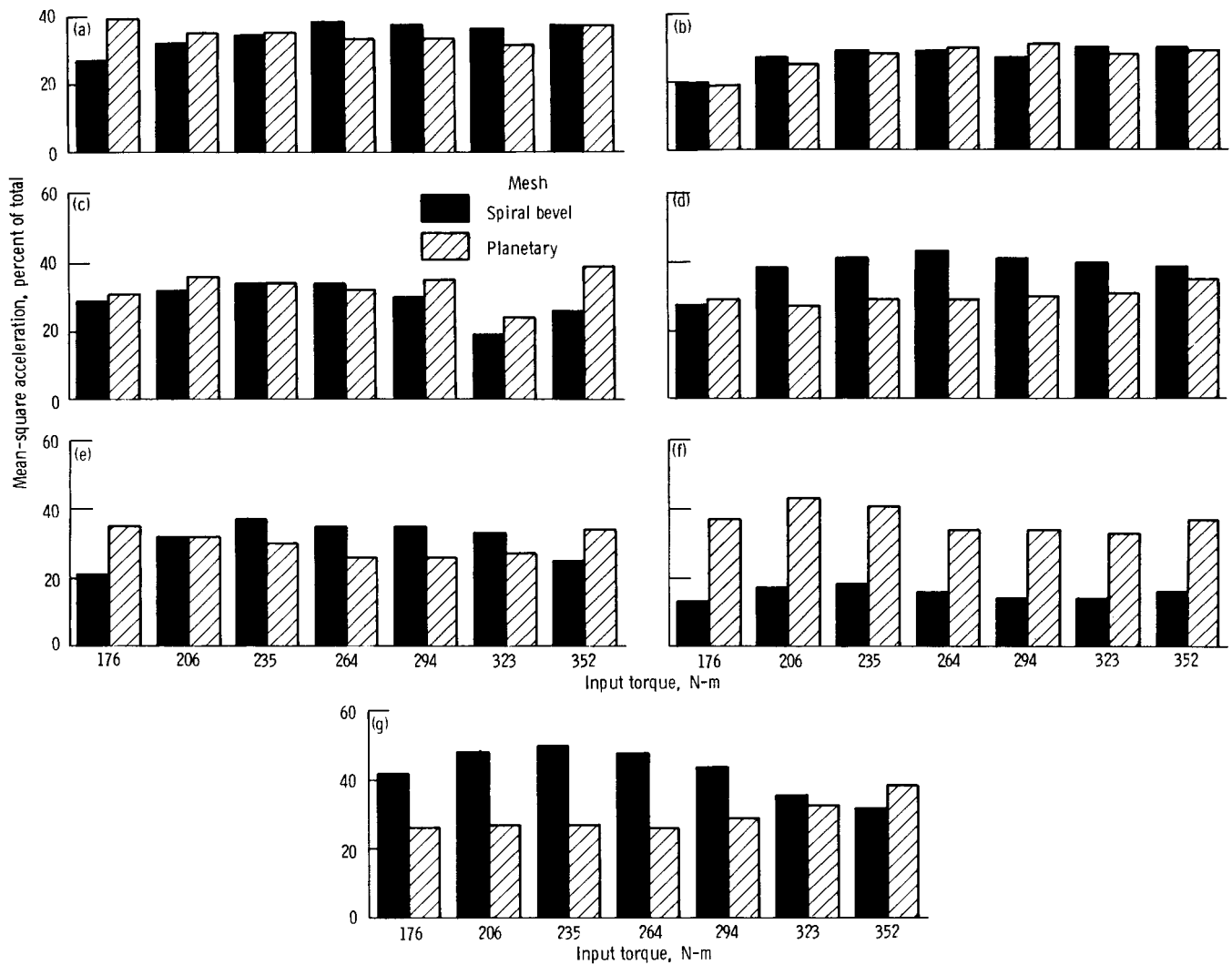


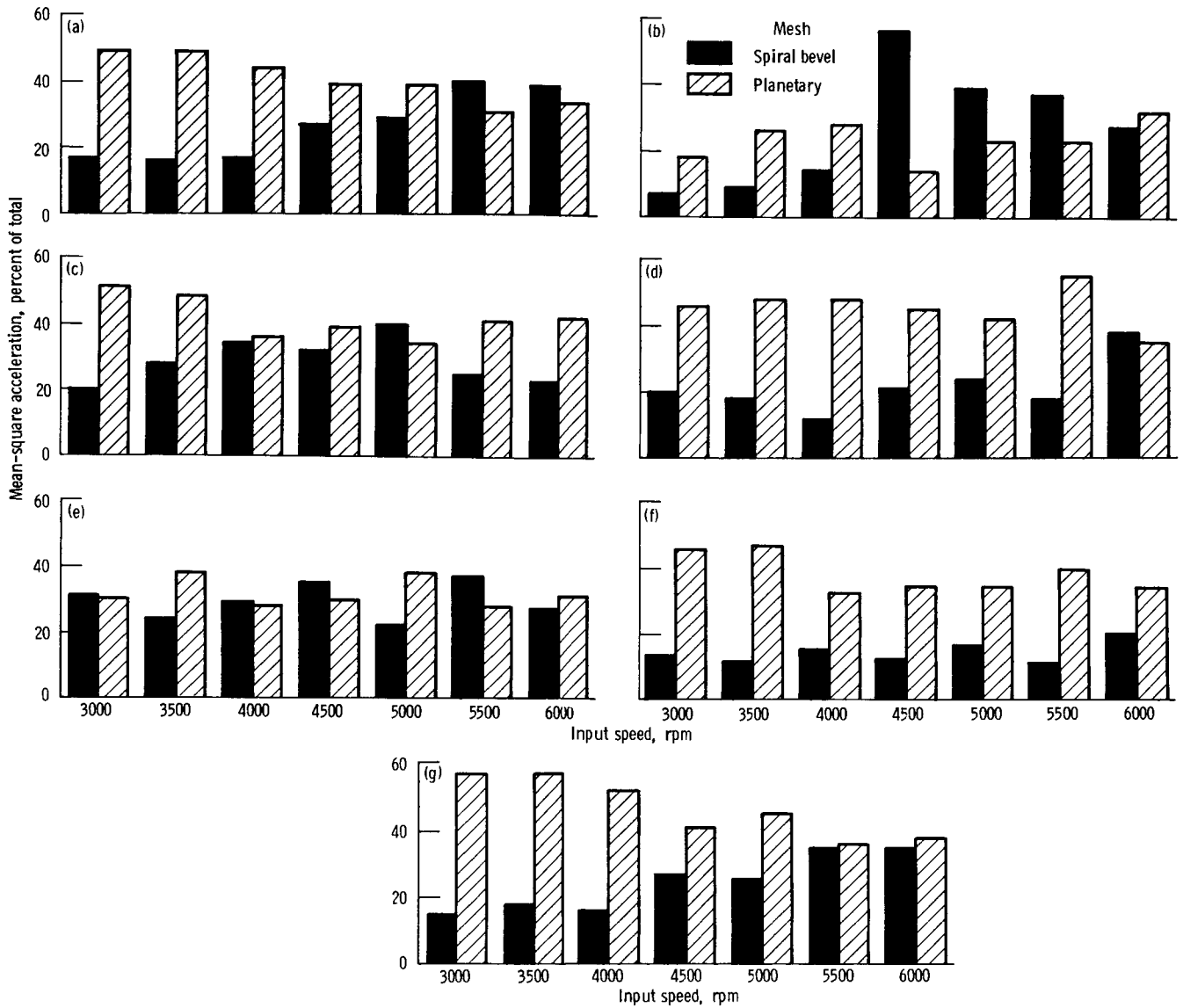
Figure 13.—Effect of speed on vibration contribution.

bevel mesh or the planetary mesh had contributed more to the vibration (figs. 14 and 15). The spiral bevel mesh contributed more than the planetary mesh in some cases (fig. 15(b) at 4500 rpm as an example), but the planetary mesh contributed more in other cases (fig. 15(g) at 3000 rpm as an example).



- (a) Accelerometer 1 (ring gear housing).
- (b) Accelerometer 2 (right trunnion mount, transverse).
- (c) Accelerometer 3 (right trunnion mount, longitudinal).
- (d) Accelerometer 4 (right trunnion mount, vertical).
- (e) Accelerometer 5 (input bevel gear housing, transverse).
- (f) Accelerometer 6 (input bevel gear housing, vertical).
- (g) Accelerometer 7 (left trunnion mount, vertical).

Figure 14.—Effect of torque on spiral bevel mesh and planetary mesh contributions to vibration.



- (a) Accelerometer 1 (ring gear housing).
- (b) Accelerometer 2 (right trunnion mount, transverse).
- (c) Accelerometer 3 (right trunnion mount, longitudinal).
- (d) accelerometer 4 (right trunnion mount, vertical).
- (e) Accelerometer 5 (input bevel gear housing, transverse).
- (f) Accelerometer 6 (input bevel gear housing, vertical).
- (g) Accelerometer 7 (left trunnion mount, vertical).

Figure 15.—Effect of speed on spiral bevel mesh and planetary mesh contributions to vibration.

Summary of Results

Experimental vibration tests were performed at NASA Lewis on the OH-58A helicopter main rotor transmission over a range of torques and speeds. Signals from accelerometers located on the transmission housing were analyzed by using Fourier spectra, power spectral density functions, and averaging techniques. The following results were obtained:

1. Transmission speed and vibration measurement location significantly affected measured rms average vibration. As speed increased, vibration generally increased, reached a maximum, and then remained fairly constant. The speed at which the measured maximum vibration occurred depended on accelerometer location.

2. The magnitude of vibration was highest at the spiral bevel gear meshing frequency.

3. Most peaks of the Fourier spectra occurred at spiral bevel gear mesh harmonics or at planetary mesh harmonics. Sideband frequencies for both spiral bevel gear harmonics and planetary harmonics occurred at multiples of the planet passing frequency.

4. Transmission torque and vibration measurement direction had a small effect on measured rms average vibration.

5. There was no trend as to the effect of torque or speed on spiral bevel gear mesh or planetary mesh vibration contributions as a percentage of total vibration.

Lewis Research Center
National Aeronautics and Space Administration
Cleveland, Ohio, January 26, 1987

Appendix—Symbols

a_k	discrete Fourier transform term, g's	m_1, m_2	slopes
B	bandwidth, Hz	N	number of gear teeth; or number of intervals, time domain
b_1, b_2	intercepts	N_r	number of ring gear teeth
b_k	discrete Fourier transform term, g's	N_s	number of sun gear teeth
f_b	spiral bevel mesh fundamental frequency, Hz	n	integer (1,2,3,...)
f_K	maximum frequency, Hz	P	number of planets
f_k	k^{th} frequency, Hz	T	time period, sec
f_m	fundamental or harmonic frequency, Hz	t	time, sec
f_p	planetary mesh fundamental frequency, Hz	$X(f_k)$	analyzer magnitude factor, g's
f_{pp}	planet passing frequency, Hz	$X'(f_k)$	discrete Fourier transform magnitude factor, g's
f_s	gear shaft frequency, Hz	$X_{\text{rms}}(f_k)$	analyzer rms average magnitude factor, g's rms
f_{side}	sideband frequency, Hz	x	acceleration, g's (zero to peak)
$G(f_k)$	one-sided power spectral density function, g's ² /Hz	x_{rms}	root-mean-square acceleration, g's rms
I	number of points	Δ	time interval between samples, sec
i	i^{th} point	ω	gear speed, rpm
j	j^{th} point	ω_s	sun gear speed, rpm
K	number of intervals, frequency domain		
k	k^{th} point		

References

1. Yoerkie, C.A.; and Chory, A.G.: Acoustic Vibration Characteristics of High Contact Ratio Planetary Gears. 40th Annual Forum, American Helicopter Society, 1984, pp. 19-32.
2. Weden, G.J.; and Coy, J.J.: Summary of Drive Train Component Technology in Helicopters. Gears and Power Transmission Systems for Helicopters and Turboprops, AGARD CP-369, AGARD, 1985, pp. 2-1 to 2-17.
3. Cornell, R.W.; and Westervelt, W.W.: Dynamic Tooth Loads and Stressing for High Contact Ratio Spur Gears. *J. Mech. Des.*, vol. 100, no. 1, Jan. 1978, pp. 69-76.
4. Mark, W.D.: Gear Noise Excitation. *Engine Noise: Excitation, Vibration, and Radiation*, R. Hickling and M.M. Kamal, eds., Plenum, 1982, pp. 55-94.
5. Drago, R.J.; and Brown, F.W.: The Analytical and Experimental Evaluation of Resonant Response in High-Speed, Lightweight, Highly Loaded Gearing. *J. Mech. Des.*, vol. 103, no. 2, Apr. 1981, pp. 346-356.
6. El-Bayoumy, L.E.: Identification and Correction of Damaging Resonances in Gear Drives. AGMA P159.05, American Gear Manufacturers Association, 1983.
7. Townsend, D.P.; Coy, J.J.; and Hatvani, B.R.: OH-58 Helicopter Transmission Failure Analysis. NASA TM X-71867, 1976.
8. Mitchell, A.M.; Oswald, F.B.; and Schuller, F.T.: Testing of YUH-61A Helicopter Transmission in NASA Lewis 2240-kW (3000-hp) Facility. NASA TP-2538, 1986.
9. Mitchell, A.M.; Oswald, F.B.; and Coe, H.H.: Testing of UH-60A Helicopter Transmission in NASA Lewis 2240-kW (3000-hp) Facility. NASA TP-2626, 1986.
10. Litvin, F.L., et al.: Spiral Bevel and Circular Arc Helical Gears: Tooth Contact Analysis and the Effect of Misalignment on Circular Arc Helical Gears. AIAA Paper 85-1139, July 1985.
11. Litvin, F.L., et al.: Generation of Spiral Bevel Gears With Zero Kinematical Errors and Computer Aided Tooth Contact Analysis. NASA TM-87273, 1986.
12. Newland, D.E.: *An Introduction to Random Vibrations and Spectral Analysis*. Longman Group Limited, London, 1975.
13. Houser, D.R.: Basis for Spectral Analysis. Fifth Turbomechanics Seminar: Spectral Analysis in Machinery Health Monitoring, National Research Council of Canada, 1978, pp. 1-1 to 1-37.
14. Bendat, J.S.; and Piersol, A.G.: *Engineering Applications of Correlation and Spectral Analysis*. John Wiley & Sons, 1980.

1. Report No. NASA TP-2705 AVSCOM TR 86-C-42	2. Government Accession No.	3. Recipient's Catalog No.	
4. Title and Subtitle Vibration Characteristics of OH-58A Helicopter Main Rotor Transmission		5. Report Date April 1987	
		6. Performing Organization Code	
7. Author(s) David G. Lewicki and John J. Coy		8. Performing Organization Report No. E-3368	
		10. Work Unit No. 505-63-51	
9. Performing Organization Name and Address NASA Lewis Research Center and Propulsion Directorate, U.S. Army Aviation Research and Technology Activity—AVSCOM, Cleveland, Ohio 44135		11. Contract or Grant No.	
		13. Type of Report and Period Covered Technical Paper	
12. Sponsoring Agency Name and Address National Aeronautics and Space Administration Washington, D.C. 20546 and U.S. Army Aviation Systems Command, St. Louis, Mo. 63120		14. Sponsoring Agency Code	
		15. Supplementary Notes David G. Lewicki and John J. Coy: Propulsion Directorate, USAARTA-AVSCOM.	
16. Abstract Experimental vibration tests covering a range of torque and speed conditions were performed on the OH-58A helicopter main rotor transmission at the NASA Lewis Research Center. Signals from accelerometers located on the transmission housing were analyzed by using Fourier spectra, power spectral density functions, and averaging techniques. Most peaks of the Fourier spectra occurred at the spiral bevel and planetary gear mesh harmonics. The highest level of vibration occurred at the spiral bevel meshing frequency. Transmission speed and vibration measurement location had a significant effect on measured vibration; transmission torque and measurement direction had a small effect.			
17. Key Words (Suggested by Author(s)) Helicopters; Transmissions; Vibration; Vibration testing; Gears; Fourier spectra; Power spectral density functions		18. Distribution Statement Unclassified—unlimited STAR Category 37	
19. Security Classif. (of this report) Unclassified	20. Security Classif. (of this page) Unclassified	21. No of pages 17	22. Price* A02